Supplementary Information

LEAD CONTACT AND MATERIALS AVAILABILITY

Further information and requests for resources and reagents should be directed to and will be fulfilled by the Lead Contact, Kevin Tsia (tsia@eee.hku.hk)

This study did not generate new unique reagents

QUANTIFICATION AND STATISTICAL ANALYSIS

In this section we describe the choice of performance measures used. For the multi-population mass cytometry datasets where relatively granular annotations where available, we adopt the approach used by Weber and Robinson 2016 and Samusik et al 2016 to compute the F1-measure as follows: First construct an F1-matrix and then apply the Hungarian algorithm to find an optimal one-to-one assignment between the manually-gated populations and the automatically detected clusters. F_{ij}=2($R_{ij}P_{ij}$)/(R_{ij} + P_{ij}) is the ij'th entry of the F1-matrix. Precision P_{ij} is the number of matches between a true class and a cluster, divided by the number of cells in that cluster; and Recall R_{ij} as the number of matches between the true label and the cluster, divided by the total number of cells for that true label (that should have been in that cluster). Precision and Recall are defined as $P_{ij} = C_{ij}/\Sigma_j(C_{ij})$, and $R_{ij} = C_{ij}/\Sigma_k(C_{kj})$ respectively. Cij is the number of cells in the i'th cluster that belong to the j'th reference population [45].

The method offers some advantages over the more common multi-class extension of the F1-score (where T is the set of true classes, $T = \{t_1, t_2, ..., t_n\}$ and S is the clustering result $= \{s_1, s_2, ..., s_m\}$.

$$F(T,S) = \sum_{t_i \in T} \frac{t_i}{N} \max_{s_j \in S} \left\{ F(t_i, s_j) \right\}$$

Most evidently, it does not bias the overall F1-measure to that found in larger populations (thus obscuring the importance of smaller but phenotypically distinct populations) and less trivially, it also avoids the problem of potentially assigning multiple reference populations to the same cluster.

However, in the absence of an adequately well annotated or detailed 'ground truth', the Hungarian method can be punitive when coarse manual gatings overlook real divisions (subpopulations) revealed by the clusters.

For the 10X PBMC scRNA-seq data as well as the Multi-ATOM data, the 'ground truth' reference annotations are coarse. To avoid penalizing the algorithm for splitting up an annotated population into distinct subtypes (e.g. a reference monocyte annotation may have been divided into clusters we can infer as classical and non-classical monocytes), we evaluate the performance evaluation based on a macro F1-score. We assign each cluster a reference label based on its majority population. This means there may be 1 or more clusters that are assigned to a particular reference population and belong to that 'macro-level' cluster. We then compute the one-vs-all F1-score for each of the major annotated populations on the 'macro-cluster' level. The mean one-vs-all F1-scores are an unweighted average to give importance to rare cells. When using the macro-F1-score, the number of clusters uncovered is reported in order to highlight that performance is achieved within a number of clusters suitable for downstream analysis.

DATA AND CODE AVAILABILITY

PARC source code is available from github: https://github.com/ShobiStassen/PARC

The mass cytometry and flow cytometry datasets (Mosmann_rare, Nilsson_rare, Samusik_all, Levine_32dim, Levine_13dim) are all publicly available at FlowRepository (repository I.D.: FR-FCM-ZZPH)

The Mouse Brain and Zheng_PBMC sc-RNA datasets are publicly available from 10X Genomics website https://www.10xgenomics.com/solutions/single-cell/

The Multi_ATOM lung cancer data supporting the current study are available from Mendeley https://data.mendeley.com/datasets/nnbfwjvmvw/draft?a=dae895d4-25cd-4bdf-b3e4-57dd31c11e37

EXPERIMENTAL MODEL AND SUBJECT DETAILS OF LUNG CANCER IMAGING FLOW CYTOMETRY DATASET

Multi-ATOM imaging protocol for Lung Cancer Data

Multi-ATOM is an ultrafast quantitative phase imaging (QPI) technique that bypasses the use of camera technology and its speed limitation. It measures the optical path length of the cell for deriving multiple biophysical markers, e.g. cell size, morphology, mass density, sub-cellular texture, refractive index etc. (Shin, S. et. al. 2018, and Lee 2019b). Detailed configuration of multi-ATOM can be referred to (K. Lee et al.,2019a and K. Lee et al., April 2019). In brief, it relies on all-optical image encoding in and retrieval from the broadband laser pulses by two mapping steps at an ultrafast line-scan rate governed by the laser repetition rate (11.8 MHz in our case): wavelength–time mapping (time-stretch process) and wavelength–space mapping (spectral-encoding process). Here the cells are in a unidirectional microfluidic flow orthogonal to the spectrally-encoded line-illumination, at a flow speed >1 m/s (equivalent to a typical imaging throughput of 10,000 cells/s). These encoded line-scans are then digitally stacked to form the

two-dimensional (2-D) images of the cells. Furthermore, by means of multiplexed spectral-encoding measurements, multi-ATOM retrieves the spatially dependent optical phase shift, or simply called *quantitative phase* from each line-scan – a quantity closely linked to variations in cell morphology and refractive index distribution that cause optical wavefront distortion as the illumination light propagates through a cell. Following our previous work (K. Lee et al., 2019a), we ensured robust in-focus single-cell imaging under a fast-microfluidic flow (>1 m/s) by designing the microfluidic channel platform to optimize the balance between the inertial lift force and the viscous drag force. The microfluidic channel was fabricated by curing polydimethylsiloxane (PDMS) on a silicon wafer mold which was prepared by the standard soft lithography technique.

The enormous number of image-context-rich multi-ATOM images favours analysis of the high-dimensional *spatially-resolved* biophysical single-cell data in large-scale. Based on the amplitude and quantitative phase images of cells, we extract the typical bulk parameters, e.g. size, averaged dry mass density (DMD), and optical opacity. Beyond that, we further transform the quantitative phase image into a 2D *dry-mass-density contrast (DC) map* and analyse its spatial variation in a statistical histogram (**Supplementary Table 5**). We note that the DC map visualizes the *local* variation of DMD within the cell. Based on the amplitude, quantitative phase and DC images, we extract in total **26** features, representing different aspects of biophysical properties of single cells.

Cell-culture of lung cancer cell lines

The 7 lung cancer cell lines consisted of 5 adherent (H358, H1975, HCC827, H520 and H2170) and 2 suspended (H526 and H69) lines. They were all cultured in their full medium: Roswell Park Memorial Institute (RPMI)-1640 with ATCC modification (Gibco^{TM}), supplemented with 10% Fetal Bovine Serum (FBS, GGibco^{TM}) and 1% Antibiotic-Antimycotic (Gibco^{TM}). The adherent types were trypsinized by 0.25% Trypsin-EDTA (Gibco^{TM}) for 4 minutes at 37^{o}C. The detached cells were extracted, centrifuged and re-suspended in complete medium. A portion would be re-seeded and the remaining (usually 1 x 10^6 ~ 3 x 10^6) suspended in 3mL of complete

medium prior to commencing the flow experiment. The suspended cell lines were centrifuged and re-suspended in complete medium. The same strategy was used to split a portion for re-seeding and the remaining were suspended in 3mL complete medium for the flow experiment. The experiment was held within 3 hours of harvesting.

KEY RESOURCES TABLE

REAGENT or RESOURCE	SOURCE	IDENTIFIER
Software and algorithms		
PARC	this paper	https://github.com/ShobiStassen/PARC-phenotyping-by-accelerated-refined-community-partitioning.git
Hierarchical Navigable Small World	Malkov and Yashunin, 2016	arXiv: 1603.09320 and https://github.com/nmslib/hnswlib
igraph	python package	https://igraph.org/python/
multicore tsne		https://github.com/DmitryUlyanov/Multicore-TSNE
Scanpy	Wolf et al. 2018	https://scanpy.readthedocs.io/en/stable/
Leiden algorithm	Traag et al. 2019	https://github.com/vtraag/leidenalg.git
Deposited data		
Samusik_all	Samusik et al (2016)	doi.org/10.1038/nmeth.3863 and doi.org/10.1002/cyto.a.23030
Levine_32dim and Levine 13dim	Levine et al (2015)	doi: 10.1016/j.cell.2015.05.047 and 10.1002/cyto.a.23030
Mosmann_rare	Mosmann et al (2014) and Weber and Robinson 2016	doi.org/10.1002/cyto.a.22445 and doi.org/10.1002/cyto.a.23030
Nilsson_rare	Nilsson et al 2013 and Weber and Robinson 2016	doi.org/10.1002/cyto.a.23030 and doi.org/10.1002/cyto.a.23030
10X PBMC	Zheng et al 2017	10.1038/ncomms14049 and www.10xgenomics.com/solutions/single-cell/
10X 1.3Million Mouse Brain	10X Genomics 2017	www.10xgenomics.com/solutions/single-cell/

Supplementary Figures

Supplementary Figure 1

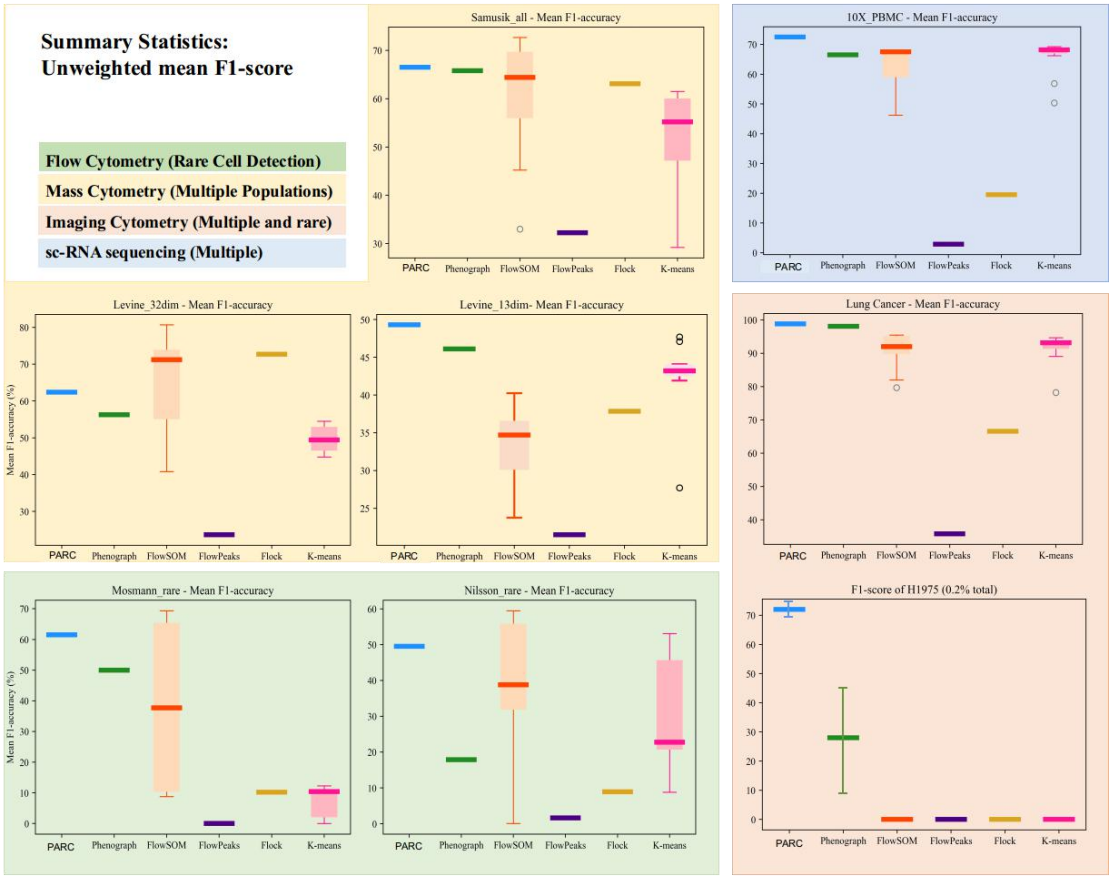

Supplementary Figure 2

Multiple population detection mean F1-Score and No. of Clusters

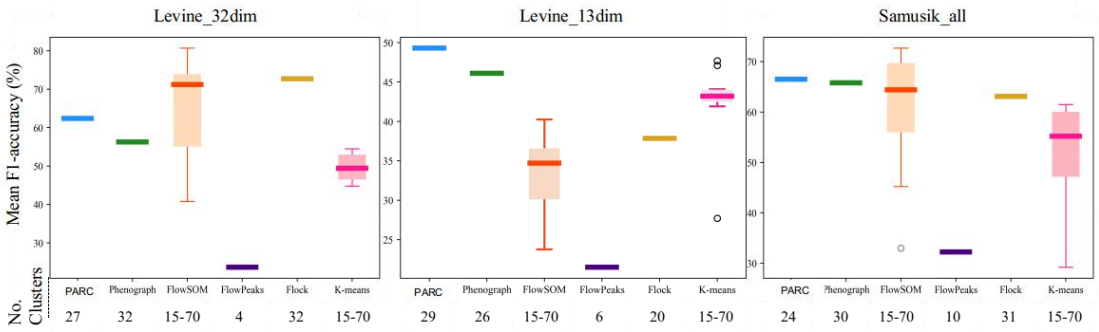

Supplementary Figure 3

Stability of Rare-cell detection of 100 H1975 cells: Phenograph vs. PARC

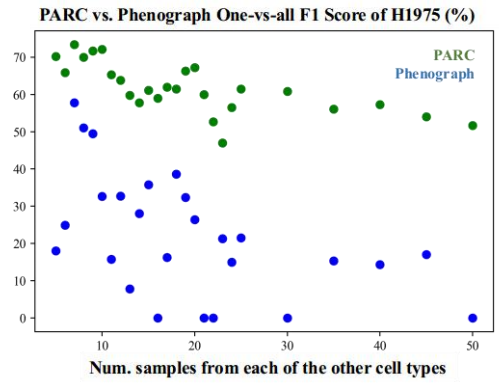

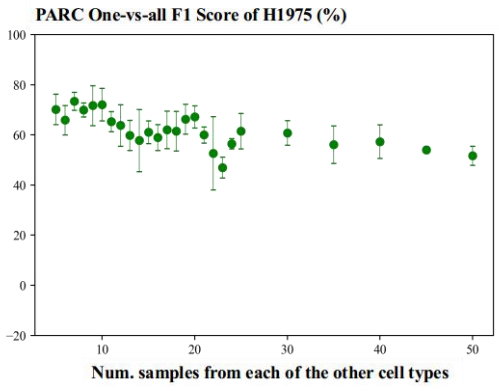

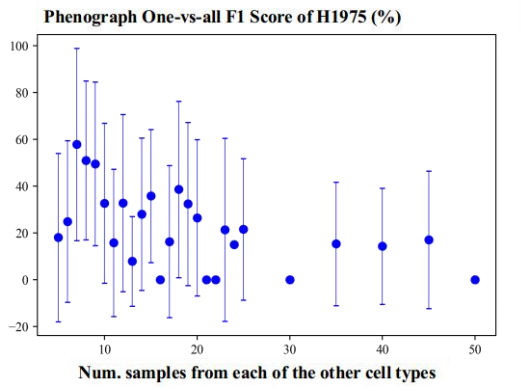

Supplementary Figure 4

"Ground Truth" annotations of 68K 10X PBMC sc-RNA data

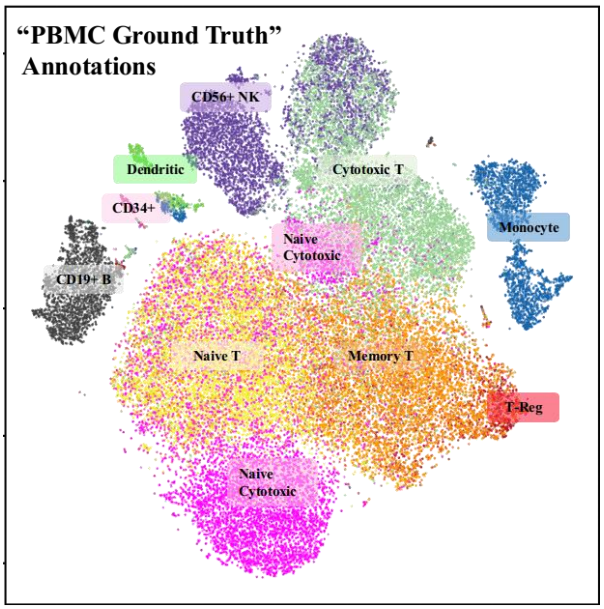

Supplementary Table 1

Performance characteristics: PARC avoids excessive fragmentation and offers significant speedup

Multi-pop	Levine_32dim N = 265K			Levine_13dim N = 167K			Samusik_All N = 841K		
	F1	**clus**	**time (s)**	**F1**	**clus**	**time (s)**	**F1**	**clus**	**time (s)**
PARC	0.63	28	90	0.49	25	35	0.66	24	331
Pheno	0.56	32	1537	0.46	27	984	0.65	30	8549
X-shift	0.69	31	11125	0.47	153	2897	0.66	74	13700

Supplementary Table 2

Pruning ensures rare populations to be consistently captured, whereas lowering K only marginally improves rare cell detection at the cost of fragmentation

Rare	**Nilsson_rare** N= 44K		**Mosmann_rare** N= 396K		**H1975 (0.04%)** N= 280,100	
Phenograph	**F1**	**clus**	**F1**	**clus**	**F1**	**clus**
K=10	0.21	39	0.15	36	0	35
K=15	0.37	33	0.46	31	0	27
K=20	0.18	30	0.49	24	0	22
K=25	0.19	28	0.48	24	0	20
K=30 (default)	0.18	26	0.50	20	0	18
PARC						
K=30 default pruning	**0.49**	**31**	**0.62**	**20**	**0.55**	**24**
K=30, no pruning	0.14	19	0.00	14	0	14
K=10, no pruning	0.18	23	0.66	19	0.24	24
K=15, no pruning	0.18	19	0.60	19	0	18
K=20, no pruning	0.15	19	0.01	16	0	19
K=25, no pruning	0.14	18	0.01	16	0	16

Supplementary Table 3

10X PBMC (68,000 cells) Marker genes and references

Markers for cell type inference			
Cluster	**Inferred Cell type**	**Markers**	**[Various Ref]**
9	Classical Monocyte	CD14+ FCGR3A- (CD16-), CX3CR1-, S100A12+	Ajami and Steinman 2018: Wong et al. (2011) ,Schinnerling et al. 2015; Stansfield and Ingram (2015)
10	Non-Classical Monocyte	CD16+, CD14+, CX3CR1+, S100A12-	
13	Myeloid and Monocyte related CD14+ Dendritic	CD1C+, CD1E+, HLA-genes, CD14	Collin et al. (2013); Wojciech (2011)
11	Plasmacytoid Dendritic	IL-3RA+ (CD123), GZMB	Collin et al. (2013); Tel et al. (2011), Zhang et al., 2017
5	NK cytotoxic CD56dimCD16+	NKG7+, FCGR3A+(CD16+), CD160+, CCR7-	Le Bouteiller et al. (2011), Hong (2012), Turman (1993)
3	NK II CD56brightCD16dim	CD160-, NKG7+	Le Bouteiller et al. (2011), Turman (1993)
8	Mature B cell	CD22+, CD79A+, CD79B+, CD19+	Boyd (2016)
17	Early-B cell	IGJ+, CD79A+	Hystad (2007), Boyd (2016)
12	CD34+Megakaryocyte	PF4+,GP9+, TREML1+, PPBP+	Sakurai (2016), Smith (2018)
6	CD25+ T-Reg	FOXP3+, CD52+, CD70+	Rudensky (2011), Samten (2013)
2	CD8+ Naive Cytoxic	CCR7+ CD8A+, CD4- CD28-, GZMK	Campbell (2001)
4,7	CD8+ CytoToxic (activated)	CD8A+, NKG7	Turman (1993)
1	CD4+ T-Memory	CD8A-, CCR7-	Campbell (2001)
16	CMV-specific CD4+ T-Memory	IFI6+, IFI27+, IFIT3	Hu (2013)
0,15,14	CD4+ Naive T	CD4+, CD8A-, CCR7+	Campbell (2001)

Supplementary Table 4

Marker Genes and references for 10X Mouse Brain (1.3 Million cells)

Cell sub-types	References
Tbr1, Eomes, Slc16a7, Slc16a7	Zeisel et al., 2018
Thalamic origin (Slc16a7)	Liguz-Lecznar and Skangiel-Kramska 2017
pyramidal projection neurons (Eomes, Tbr1)	Hevner et at., 2006
Cortical Terminals (Slc16a6)	Liguz-Lecznar and Skangiel-Kramska 2017
Aldoc, Hes1, Olig1, Gja1, Gfap	
Aldoc, Gfap (astrocyte)	Tasic et al., 2016 Boisvert et al., 2018
Olig1 (oligdendrocyte)	Othman te al., 2011
Hes1 (Glia)	Furukawa et al., 2000
Gad1, Gad2, Slc32a1	Tasic et al., 2016
Sst (SOM interneuron)	Gonchar et al., 2007
Calcr (CR interneuron)	Reynolds and Beasley 2001
Calb1 (CB interneuron)	Reynolds and Beasley 2001
Htr3a (cortical interneuron)	Frazer et al., 2017

Supplementary Table 5

Population composition of PARC's clustering of Lung Cancer multi-ATOM data

Cell type	Major cell line	Cell count
h2170-0	squamous	167662
h2170-2	squamous	129825
h526-13	small cell	31058
h520-1	squamous	154626
h520-3	squamous	126852
h520-4	squamous	60130
h520-5	squamous	57626
h358-6	Adenocarcinoma	53719
h358-9	Adenocarcinoma	39385
h358-11	Adenocarcinoma	33653
h358-16	Adenocarcinoma	22751
h69-10	small cell	35884
h69-14	small cell	28802
h827-7	Adenocarcinoma	47259
h827-8	Adenocarcinoma	45029
h1975-12	Adenocarcinoma	30069
h1975-15	Adenocarcinoma	22648

Supplementary Table 6

Description of biophysical features extracted from multi-ATOM images

Biophysical features summary

Feature	QPI/BF	Description
Area/Volume	BF	Linked to cell proliferation and growth and often used in conjunction with cell mass to study regulation of cell size (Girshovitz and Shaked 2012)
Circularity	BF	Measure of conic deviation from cell being circular. Can be indicative of cell apoptosis or disease mass to study regulation of cell size (Girshovitz and Shaked 2012)
Attenuation Density	BF	Indicative of cell composition
Amplitude (Moments)	BF	Peak, mean and variance of BF amplitude
Dry Mass Density	QPI	Mass of non-aqueous material of cell, which is the integral of the optical path delay profile on the projected cell area. mass to study regulation of cell size (Girshovitz and Shaked 2012)
Dry Mass Density Contrast (Moments)	QPI	Statistical features of DMD contrast which measures local variations in DMD (Lee 2018)
Phase Arrangement (Moments)	QPI	Extract spatial phase information by considering the distribution of the phase as a function of the radius (distance from image center)
Phase orientation	QPI	Distribution of the phase as a function of a product of the angle and radius (from center of image)

BF: bright-field; QPI: quantitative phase image; DMD: dry-mass density

REFERENCES

Ajami B. and Steinman L. (2018) Nonclassical monocytes: are they the next therapeutic targets in multiple sclerosis? Australas. Soc. Immunol. Inc., 96, 125–127.

Boisvert M.M. et al. (2018) The aging astrocyte transcriptome from multiple regions of the mouse brain. Cell Rep., 22, 269–228.

Boyd, Scott D et al. (2013) "Selective immunophenotyping for diagnosis of B-cell neoplasms: immunohistochemistry and flow cytometry strategies and results." Applied immunohistochemistry & molecular morphology : AIMM vol. 21,2 : 116-31.

Campbell J.J. et al. (2001) CCR7 expression and memory T cell diversity in humans. J. Immunol., 166, 877–884.

Collin M. et al. (2013) Human dendritic cell subsets. Immunology, 140, 22–30.

Le Bouteiller P. et al. (2011) CD160: a unique activating NK cell receptor. Immunol. Lett., 138, 93–96.

Frazer S. et al. (2017) Transcriptomic and anatomic parcellation of 5-HT3AR expressing cortical interneuron subtypes revealed by single-cell RNA sequencing. Nat. Commun., 8, 14219.

Furukawa T. et al. (2000) Rax, Hes1, and notch1 promote the formation of Müller glia by postnatal retinal progenitor cells. Neuron, 26, 383–394.

Gonchar Y. et al. (2007) Multiple distinct subtypes of GABAergic neurons in mouse visual cortex identified by triple immunostaining. Front. Neuroanat., 1, 3.

Hevner R.F. et al. (2006) Transcription factors in glutamatergic neurogenesis: conserved programs in neocortex, cerebellum, and adult hippocampus. Neurosci. Res., 55, 223–233.

Hong H.S. et al. (2012) Loss of CCR7 expression on CD56bright NK cells is associated with a CD56dimCD16+ NK cell-like phenotype and correlates with HIV viral load. PLoS ONE 7(9): e44820.

Hu H. et al. (2013) Distinct gene-expression profiles associated with the susceptibility of pathogen-specific CD4 T cells to HIV-1 infection. Blood, 121, 1136–1144.

Hystad M.E. (2007) Characterization of early stages of human B cell development by gene expression profiling. J. Immunol., 79, 3662–3671.

Liguz-Lecznar M. and Skangiel-Kramska J. (2007) Vesicular glutamate transporters (VGLUTs): the three musketeers of glutamatergic system. Acta Neurobiol. Exp., 67, 207–218.

Levine J.H. et al. (2015) Data-driven phenotypic dissection of AML reveals progenitor-like cells that correlate with prognosis. Cell, 162, 184–197.

Lee K.C.M. et al. (2019a) Multi-ATOM: ultrahigh-throughput single-cell quantitative phase imaging with subcellular resolution. J. Biophotonics, 12, e201800479.

Lee K.C.M. et al. (2019b) Quantitative phase imaging flow cytometry for ultra-large-scale single-cell biophysical phenotyping. Cytometry A, 95, 510–520.

Malkov Y. and Yashunin D. (2016) Efficient and Robust Approximate Nearest Neighbor Search using Hierarchical Navigable Small World Graphs. In: IEEE Transactions on Pattern Analysis and Machine Intelligence. doi: 10.1109/TPAMI.2018.2889473.

Mosmann T.R. et al. (2014) SWIFT—Scalable clustering for automated identification of rare cell populations in large, high-dimensional flow cytometry datasets, part 2: biological evaluation. Cytometry, 85A, 422–433

Nilsson A.R. et al. (2013) Frequency determination of rare populations by flow cytometry: a hematopoietic stem cell perspective. Cytometry A, 83A, 721–727.

Othman A. et al. (2011) Olig1 is expressed in human oligodendrocytes during maturation and regeneration. Glia, 59, 914–926.

Reynolds G.P. and Beasley C.L. (2001) GABAergic neuronal subtypes in the human frontal cortex development and deficits in schizophrenia. J. Chem. Neuroanat., 22, 95–100.

Rudensky A. (2011) Regulatory T cells and Foxp3. Immunol. Rev., 241, 260–268.

Samten B. (2013) CD52 as both a marker and an effector molecule of T cells with regulatory action: identification of novel regulatory T cells. Cell. Mol. Immunol., 10, 456–458.
Sakurai K. et al. (2016) Inhibition of human primary megakaryocyte differentiation by anagrelide: a gene expression profiling analysis. Int. J. Hematol., 104, 190–199.
Samusik N. et al. (2016) Automated mapping of phenotype space with single-cell data. Nat. Methods, 13, 493–496.

Schinnerling K. et al. (2015) Gene expression profiling of human monocyte-derived dendritic cells – searching for molecular regulators of tolerogenicity. Front. Immunol., 6, 528.

Shin, S., Kim, D., Kim, K. et al. Super-resolution three-dimensional fluorescence and optical diffraction tomography of live cells using structured illumination generated by a digital micromirror device. Sci Rep 8, 9183 (2018).

Smith C.W. et al. (2018) TREM-like transcript 1: a more sensitive marker of platelet activation than P-selectin in humans and mice. Blood Adv., 2, 2072–2078.

Stansfield B.K. and Ingram D.A. (2015) Clinical significance of monocyte heterogeneity. Clin. Transl. Med., 4, 5.

Tasic B. et al. (2016) Adult mouse cortical cell taxonomy by single cell transcriptomics. Nat. Neurosci., 19, 335–346.

Tel J. et al. (2011) IL-4 and IL-13 alter plasmacytoid dendritic cell responsiveness to CpG DNA and herpes simplex virus-1. J. Invest. Dermatol., 131, 900–906.

Traag V.A. et al. (2019) From Louvain to Leiden: guaranteeing well-connected communities. Sci. Rep., 9, 5233.

Turman M.A. et al. (1993) Characterization of a novel gene (NKG7) on human chromosome 19 that is expressed in natural killer cells and T cells. Hum. Immunol., 36, 34–40.

Weber L.M. and Robinson M.D. (2016) Comparison of clustering methods for high-dimensional single-cell flow and mass cytometry data. Cytometry A, 89, 1084–1096.

Wong K.L. et al. (2011) Gene expression profiling reveals the defining features of the classical, intermediate, and nonclassical human monocyte subsets. Blood, 118, e16–e31.

Wolf F.A. et al. (2018) SCANPY: large-scale single-cell gene expression data analysis. Genome Biol., 19, 15.

Zeisel A. et al. (2018) Molecular architecture of the mouse nervous system. Cell, 174, 999–1014.

Zheng G.X.Y. et al. (2017) Massively parallel digital transcriptional profiling of single cells. Nat. Commun., 8, 14049.